



# Temperature and frequency dependent dielectric capacitance and polarization performances of low dimensional perovskite based manganese stannate

Sarit K. Ghosh<sup>1,\*</sup>, and Kaushik Mallick<sup>1,\*</sup>

<sup>1</sup> Department of Chemical Sciences, University of Johannesburg, P.O. Box 524, Auckland Park 2006, South Africa

Received: 18 July 2023

Accepted: 13 August 2023

© The Author(s), 2023

## ABSTRACT

Manganese stannate perovskite nanoparticles were synthesized by applying a complexation mediated approach. Rietveld refinement of the XRD data exhibited orthorhombic structure with space group of  $Pnma$ . The structure included eightfold coordinated  $Mn^{2+}$  cation, surrounded by eight  $O^{2-}$  anions and formed  $MnO_8$  polyhedra unit. Each polyhedra unit interconnected through the corner-sharing  $SnO_6$  octahedra with the formation of a cage-like network. The temperature and frequency dependent dielectric performances of manganese stannate were measured in the form of a device, which exhibited maximum dielectric constant value  $\sim 3445$ . The high dielectric constant value was originated due to the contribution of space charge polarization and orientation polarization of dipoles within the measured frequency ranges. Temperature and frequency dependent AC-conduction mechanism of the manganese stannate-based device involved both overlapping large polarons and non-overlapping small polarons. Electric field-dependent of polarization hysteresis loop of the device exhibited the maximum polarization value  $1.5 \mu C/cm^2$  under the electric field of 3 kV/mm. Under the applied field of 2 kV/mm, the device exhibited a fatigue-free polarization with a maximum value of  $0.92 \mu C/cm^2$ , sustained for  $10^3$  cycles under ambient temperature condition.

## 1 Introduction

Stannate-based materials exhibited a wide range of physical properties, rendering them highly suitable for utilization in various electronic devices [1–3]. Such kind of ternary oxides are chemically stable and have attracted significant attention due to their versatile performances. Lanthanum-doped  $BaSnO_3$  showed technological potential for non-volatile electronic devices [4]. The investigation of  $ZnSnO_3$  nanostructures was

undertaken by researchers in order to explore their potential implementation in piezoelectric devices owing to their notable polarization characteristic. A scientific study unveiled that the composite of polydimethyl siloxane and  $ZnSnO_3$  nanostructure synergistically functioned as a nanogenerator, exhibiting the capacity to energetically sustain light-emitting diodes and other electronic devices [5]. Asymmetric supercapacitor based on nickel stannate and ferrous stannate demonstrated significant potential for enabling

Address correspondence to E-mail: saritghosh@gmail.com; kaushikm@uj.ac.za

self-powered wearable device [6]. Li-ion transport property of Li-doped  $\text{SrSnO}_3$  exhibited lower diffusion activation energy and higher diffusivity, implying the potential of the material for Li-ion battery application [7]. The remarkable electrical conductivity and excellent transparency exhibited by the  $\text{Cd}_2\text{SnO}_4$  film make it highly desirable for applications in solar energy harvesting processes [8]. It is reported that perovskite  $\text{BaSnO}_3$  and  $\text{SrSnO}_3$  display strong luminescence and photocatalytic performance, respectively [9, 10]. Neodymium-doped  $\text{SrSnO}_3$  has been reported for the development of high-power electronic devices [11]. Perovskite structure of  $\text{ASnO}_3$  ( $A = \text{Ba}, \text{Sr}$ ) have superior electron conductivity that rendering them as promising candidates for transparent conducting oxides [12]. Among the various perovskite stannate-based materials [13],  $\text{PbSnO}_3$  demonstrated spontaneous polarization and moderate dielectric constant value under an external applied field, however, responded differently for titanate containing  $\text{Sn}^{4+}$  ions,  $\text{Pb}(\text{Ti-Sn})\text{O}_3$ , that influenced the dielectric anomalies and ferroelectric polarization within the system [14]. Perovskite structure of  $\text{ZnSnO}_3$  has attracted much attention for its unique properties of optical transparency [15], ferroelectric [16] and field-effect transistor applications [17]. It was reported that organic molecule stabilized  $\text{ZnSnO}_3$  hybrid structure exhibited better electro-mechanical stress, flexibility, polarization and piezoelectric properties than conventional zinc stannate system [18]. Experimental and theoretical studies revealed that the polarizability of organic molecule alters the structural and electrical performances of the  $\text{ZnSnO}_3$  material [18].

Non-perovskite silver stannate ( $\text{Ag}_2\text{SnO}_3$ ) nanocrystal with linear arrangement of Ag-atoms along the c-axis demonstrated the high value of electrical conductivity with low dielectric breakdown strength and polarizability under an applied electric field [19]. However, the dielectric and polarization strength of  $\text{Ag}_2\text{SnO}_3$  nanocrystal was improved significantly due to the incorporation of carbon nitride in the system that prevents the formation of silver filament [19]. Amorphous  $\text{CoSnO}_3@\text{C}$  system exhibited an excellent cycle life and improved rate capability for lithium-ion batteries when applied as an anode material [20]. Graphene oxide decorated  $\text{CoSnO}_3@\text{ZnSnO}_3$  system showed high energy storage and capacity retention performance for asymmetric supercapacitor application [21]. Composite system of  $\text{NiSnO}_3$ -graphene displayed as high-performance electrode towards

asymmetric supercapacitor application [22]. Acid mediated formation of  $\text{CuSnO}_3$  nanoparticles showed photocatalytic and antibacterial applications [23].

High pressure synthesis route was reported for the preparation of manganese stannate ( $\text{MnSnO}_3$ ) perovskite system that showed magnetodielectric coupling and multiferroic properties under the magnetic field [24]. The above system exhibited dielectric constant value of  $\sim 22$  at 300 K under 100 kHz and zero magnetic field condition. Studies revealed that the ferroelectric phase transition and polarization under external pressure caused the structural distortion of  $\text{MnSnO}_3$  system [25, 26]. The distortion in the Mn–O bond length was responsible for the elongation of  $\text{SnO}_6$  octahedra unit that improved the field induced polarization behaviour of the material [26]. Amorphous  $\text{MnSnO}_3$  also functioned as high-performance electrode materials with superior rate capability and long-term cyclic life for lithium storage systems [27]. Ferroelectric  $\text{MnSnO}_3$  was identified as a possible candidate for photovoltaic application due to its small band gap and excellent carrier mobility [28].

In the present study, complexation strategy was applied to synthesis the single phase orthorhombic manganese stannate ( $\text{MnSnO}_3$ ) nanoparticles under ambient temperature and pressure conditions. The Rietveld refinement analysis was performed based on the experimental diffracted data of  $\text{MnSnO}_3$  system. A device, based on  $\text{MnSnO}_3$ , was fabricated on a flexible substrate and measured the dielectric capacitance, AC-conductivity and electric field dependent polarization under wide range of temperature and frequency conditions. Electrical mobility and polarization performance of the device was correlated with polaron and vacancy mediated mechanisms, respectively.

## 2 Experimental sections

### 2.1 Materials

$\text{MnCl}_2 \cdot 4\text{H}_2\text{O}$ ,  $\text{K}_2\text{SnO}_3$ ,  $3\text{H}_2\text{O}$  and hexamethylenediamine were used in this study without any further purification.

### 2.2 Synthesis of manganese stannate (MSO) nanoparticles

In a typical synthesis process, 0.12 g of hexamethylenediamine (HMDA) was dissolved in 10 mL of methanol

in a conical flask. An aqueous solution of manganese chloride (10 mL) with the concentration of  $0.1 \text{ mol/dm}^3$  was slowly added to the solution of HMDA, leading to the subsequent formation of a complex of Mn(II)-HMDA with a deep brown colour. The addition of 5 mL of  $\text{K}_2\text{SnO}_3 \cdot 3\text{H}_2\text{O}$  ( $0.1 \text{ mol/dm}^3$ ) dropwise to the complex resulted in the formation of a solid black precipitate at the bottom of the conical flask. The synthesized material was filtered and dried at  $80^\circ\text{C}$  under vacuum. The structural property of the synthesized material was characterized using X-ray diffraction (Philips PANalytical), Raman (Jobin–Yvon T64000) and X-ray photoelectron spectroscopy (VG Multilab 2000) techniques that confirmed the formation of manganese stannate ( $\text{MnSnO}_3$ ).

### 2.3 Device fabrication and characterization

The flexible manganese stannate (MSO)-based device was fabricated on an indium tin oxide (ITO) coated PET (polyethylene terephthalate) substrate. Initially, a slurry was made by mixing manganese stannate with chloroform and deposited, using a drop-and-dry method, on the ITO substrate, acted as a working (bottom) electrode. The deposited material was dried and coated with gold on the top side of the material (top electrode) using the physical vapour deposition technique (EMSCOPE SC 500). The fabricated MSO-based device has a dimension with the thickness of  $\sim 100 \mu\text{m}$  and the electrode area of  $\sim 21 \text{ mm}^2$ . The electrical studies of the fabricated device were performed under different temperature and frequency conditions.

The temperature and frequency dependent dielectric and polarization performances of the MSO-based device were measured using HP 4284A LCR meter and Sawyer–Tower circuit interfaced with computer controlled temperature chamber. A triangular waveform of frequency 10 Hz was applied to the device for polarization–electric field (P-E) study under varying temperature condition.

## 3 Results and discussion

The X-ray diffraction pattern of manganese stannate, Fig. 1A, recorded within the range ( $2\theta$ ) from  $20^\circ$  to  $80^\circ$ . The diffracted pattern of the synthesized material is similar with an isostructural perovskite  $\text{SrSnO}_3$  structure [29–31]. Sharp and well defined diffracted peaks revealed the formation of single phase manganese

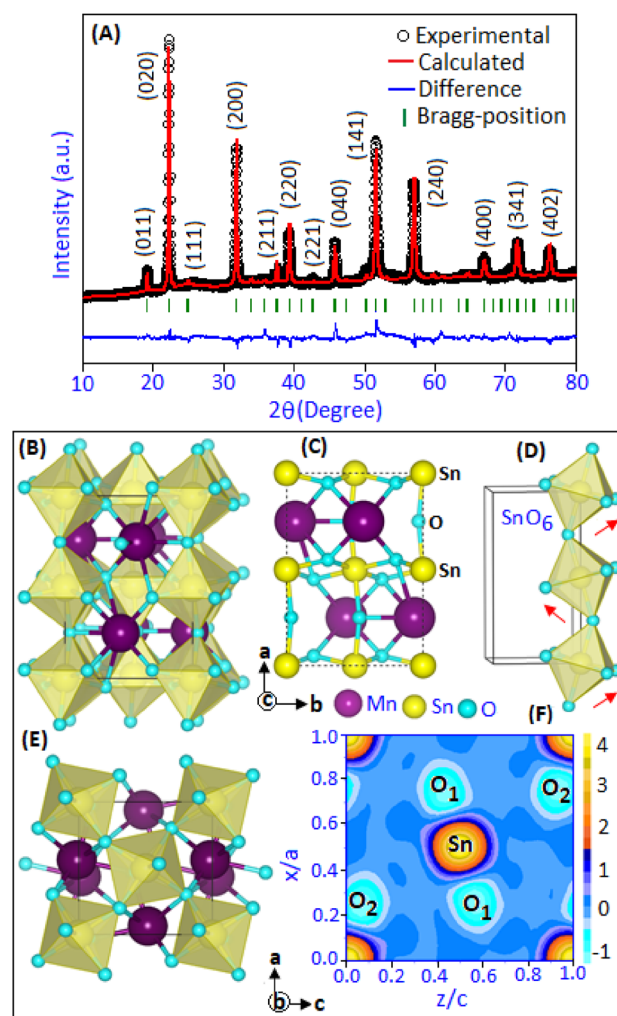


**Fig. 1** A Rietveld refinement pattern for manganese stannate. The symbol (black circle) is the experimental curve; red solid line is the calculated, blue solid line is the difference between experimental and calculated pattern, green vertical bars are the Bragg-positions of orthorhombic phase. B and C Unit cell representation of manganese stannate projected along c-axis and D represents the tilting in  $\text{SnO}_6$  octahedra unit. E and F Represents the unit cell projection along b-axis and the equivalent electron density mapping of the material (Color figure online)

stannate. The Rietveld refinement analysis was performed on the experimental diffracted (black circle) data of  $\text{MnSnO}_3$  system. The overall diffracted pattern was refined according to the orthorhombic crystal structure with the space group of  $\text{Pnma}$  (No. 62). The vertical bar (green colour) represents the Bragg-position of the lattice symmetry. The calculated diffraction pattern (red line) and the corresponding difference (blue line) are attained within the acceptable range of

convergent factor ( $\chi^2 = 1.5$ ,  $R_{wp} = 6.2\%$  and  $R_p = 4.4\%$ ). The refined lattice parameters,  $a = 5.55$  (6) Å,  $b = 5.54$  (4) Å,  $c = 7.85$  (4) Å and  $\alpha = \beta = \gamma = 90^\circ$  are obtained from the refinement analysis. The detail structural parameters such as atomic positions, lattice occupancy,  $B_{iso}$ , X-ray density and bond length of the  $MnSnO_3$  system are listed in Table S1 (Supporting information). The observed diffraction pattern revealed the formation of single-phase of  $MnSnO_3$ . The unit cell representation of  $MnSnO_3$  system was constructed using the refined lattice parameters, Fig. 1B. The structure consists of eightfold coordinated  $Mn^{2+}$  cation, surrounded by eight  $O^{2-}$  anions and formed  $MnO_8$  polyhedra unit. Each polyhedra unit interconnected with the corner-sharing  $SnO_6$  octahedra with a cage-like network [32, 33] (Fig. S1A, supporting information). Within the unit cell, the oxygen ion is linearly coordinated with two  $Sn^{4+}$  cations in Sn–O–Sn arrangement and enclosed with four  $Mn^{2+}$  cations in a plane, perpendicular to Sn–O–Sn bond, Fig. 1C. The  $MnSnO_3$  structure involved an in-plane tilting of  $SnO_6$  octahedral unit along the  $c$ -axis, as highlighted (red arrows) in Fig. 1D and that created a distortion on the local charge distribution. The local charge density mapping of  $MnSnO_3$  unit cell projected along the  $b$ -axis, Fig. 1E, was constructed by using G-Fourier 2D contour plot (FullProf software), Fig. 1F. Yellow colour on the charge density scale corresponds to the maximum charge accumulation at Sn-atom site in comparison with oxygen,  $O_1$  and  $O_2$ , (cyan colour) site. The structural stability of orthorhombic manganese stannate was verified from the tolerance factor ( $t \sim 0.80$ ) using Goldschmidt formula (equation S1, supporting information). The deviation of  $t$ -factor, from ideal value of cubic perovskite ( $t \sim 1$ ), justified the structural distortion of  $SnO_6$  or  $MnO_8$  units, which yielded the lower symmetrical arrangement of  $MnSnO_3$ . Similar value of tolerance factor has been reported in other orthorhombic perovskite systems with smaller cationic radii [33–35].

The transmission electron microscope (TEM, JEOL JEM-2100) image, Fig. 2A, shows cube-like morphology of manganese stannate within the size range between 50 and 70 nm. Higher magnification TEM image, Fig. 2B, displays the prominent edges of cubic shaped stannate particle. The selected area electron diffraction (SAED) pattern, Fig. 2C, confirms the crystalline nature of the nanocubes, manifested by regular order of the diffraction spots.

Raman spectrum of manganese stannate was measured within the frequency range from 50 to 850  $cm^{-1}$ ,

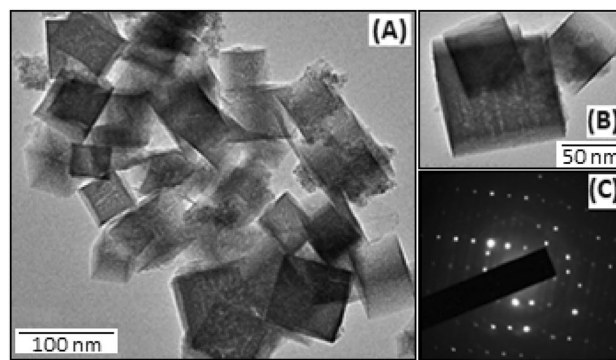


**Fig. 2** A and B Transmission electron microscope images of manganese stannate nanoparticles under different magnification. C The selected area electron diffraction pattern of the nanoparticle

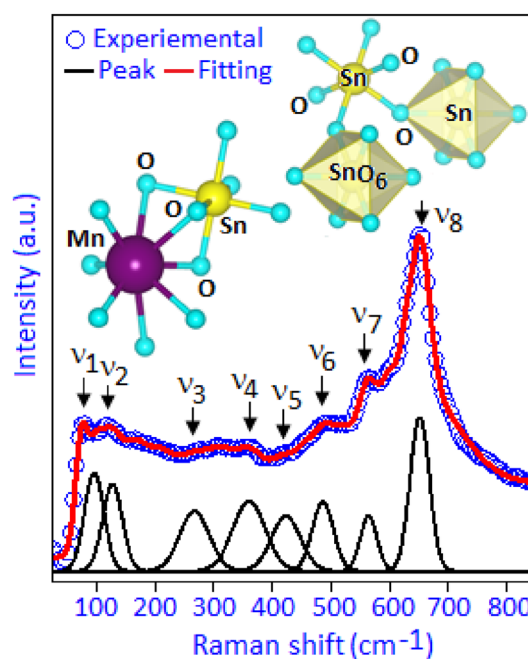


**Fig. 3** Raman spectra of manganese stannate, measured within the frequency range from 50 to 850  $cm^{-1}$ . The spectrum was deconvoluted (black colour) in eight Raman active modes ( $\nu_1$ – $\nu_8$ ) (Color figure online)

Fig. 3. The spectrum was deconvoluted (black colour) into eight Raman active modes ( $\nu_1$  to  $\nu_8$ ). At the low frequency region (50–150  $cm^{-1}$ ), the Raman peak positioned at  $\nu_1 \sim 94.3$   $cm^{-1}$  and  $\nu_2 \sim 126.3$   $cm^{-1}$  are correspond to soft lattice mode, designated as  $A_g$  and  $B_{2g}$  respectively, originated from the  $Mn-SnO_3$  vibrations [29, 36]. The  $\nu_1$  mode is associated with the bending of O–Sn–O bond, along with the vibration of  $Mn^{2+}$

cation. At intermediate frequency range, other diffuse modes ( $B_{2g}$ ) positioned at  $\nu_3 \sim 260 \text{ cm}^{-1}$ ,  $\nu_4 \sim 359.0 \text{ cm}^{-1}$  and  $\nu_5 \sim 423 \text{ cm}^{-1}$  correspond to the Sn–O–Sn scissoring vibration, bending of Sn–O and torsional mode of  $\text{SnO}_3$  unit, respectively [29]. The torsional mode ( $\text{SnO}_3$ ) is further observed as a shoulder like feature in the spectrum, positioned at  $\nu_6 \sim 486.8 \text{ cm}^{-1}$  and  $\nu_7 \sim 570 \text{ cm}^{-1}$ . Both  $\nu_6$  and  $\nu_7$  vibration modes are associated with the stretching and bending motion of Sn–O and O–Sn–O bonds, respectively [37]. The intense mode at  $\nu_8 \sim 653.2 \text{ cm}^{-1}$  is the signature of  $\text{SnO}_6$  octahedra, which is the originated from the stretching vibration of the unit. The off-centre displacement of  $\text{Sn}^{4+}$  cation is responsible for net polarization behaviour of the stannate based perovskite system and is evident from the  $\nu_8$  mode [28, 38].

X-ray photoelectron spectroscopy (XPS) technique was applied to determine the elemental composition and oxidation states of manganese stannate system. Figure 4A exhibits the survey spectrum that confirm the presence of C, N, Mn, Sn and O elements. The presence of C and N originated from hexamethylenediamine, acted as stabilizer. Figure 4A, inset, shows the high-resolution C 1 s and N 1 s spectra. The C 1 s spectrum, after deconvolution, displays the main peak at 285.3 eV, assigned for C–C bond (pink area) and the green area with a peak positioned at 286.2 eV corresponds to C–N bond. For N 1 s spectra, the peak at 399.5 eV is associated with the nitrogen from  $-\text{NH}_2$  group of hexamethylenediamine. Figure 4B, displays high resolution XPS-spectrum of deconvoluted Mn 2p with the spin–orbit splitting components  $2p_{1/2}$  and  $2p_{3/2}$ , positioned at 653.7 eV and 642.2 eV, respectively, with a shake-up peak at 645.30 eV, associated with the  $\text{Mn}^{2+}$  oxidation state [39–41]. The oxidation state of Mn cation is more accurately identified by the Mn 3 s spectrum, Fig. 4C. It was reported that the exchange interaction between the core-level 3 s electron and the unpaired electrons in the 3d valence band causes a separation in the binding energy ( $\Delta E$ ) of Mn 3 s spectra [41]. The present spectra of Mn-3 s exhibit two well defined peaks positioned at 89.8 eV and 84.0 eV with a separation of binding energy  $\Delta E \sim 5.8 \text{ eV}$ , confirmed the presence of  $\text{Mn}^{2+}$  oxidation state for the title material. High-resolution Sn 3d spectra, Fig. 4D, shows two characteristic peaks at 495.1 and 486.6 eV corroborate with Sn  $3d_{3/2}$  and Sn  $3d_{5/2}$ , respectively, indicates the presence of  $\text{Sn}^{4+}$  oxidation state. The deconvoluted O 1 s spectra, Fig. 4E, fitted into two Gaussian peaks and the main peak positioned at  $\sim 529.5 \text{ eV}$  (pink colour)

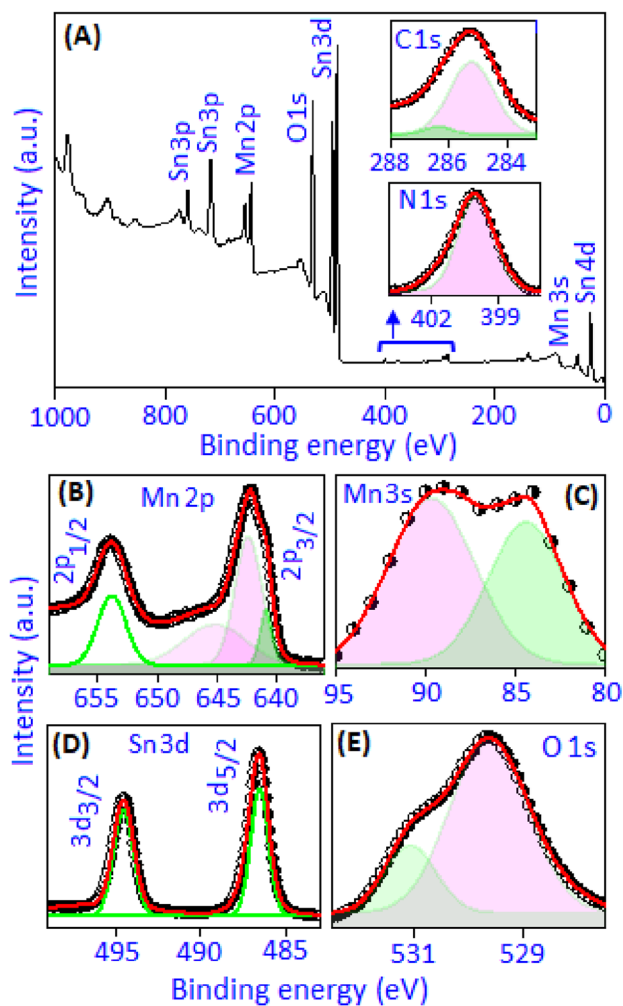
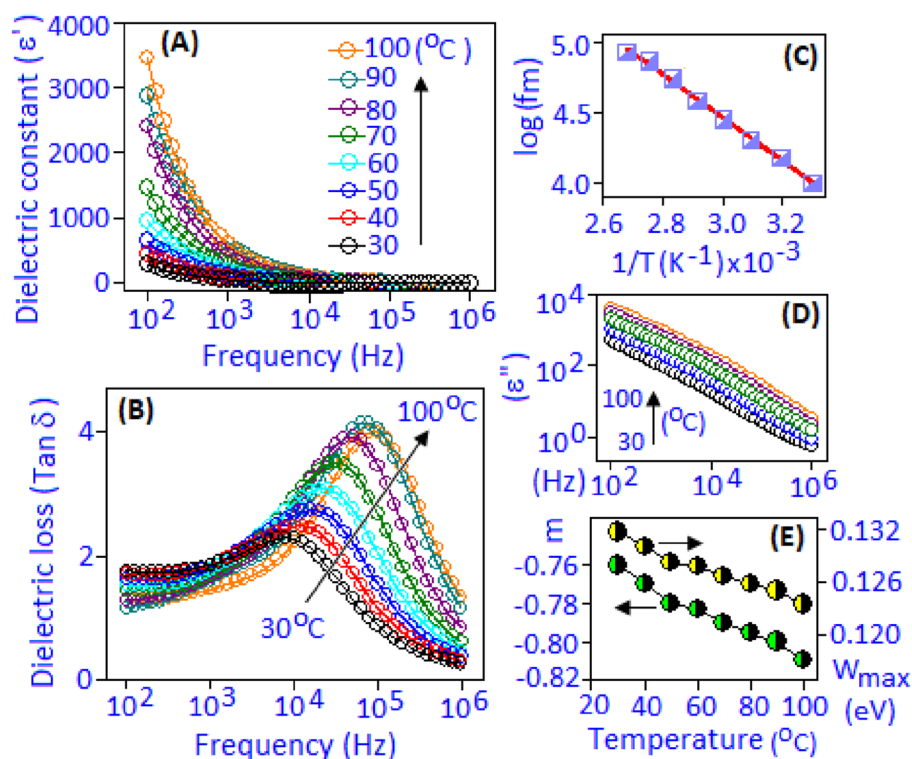


**Fig. 4** A The XPS survey spectrum of the  $\text{MnSnO}_3$  system. Inset figures show C 1 s and N 1 s spectrum. High resolution deconvoluted spectrum of B Mn 2p, C Mn 3 s, D Sn 3d and E O 1 s

contributed from the lattice oxygen, whereas the other diffuse peak  $\sim 531.3 \text{ eV}$  (green colour) is due to the presence of oxygen vacancy in the manganese stannate system [42].

The Temperature ( $30\text{--}100 \text{ }^\circ\text{C}$ ) and frequency (from 100 Hz to 1 MHz) dependent dielectric performances of manganese stannate (MSO) was measured in the form of a device. The real part of the dielectric constant ( $\epsilon'$ ) under different temperature condition is shown in the Fig. 5A. At  $30 \text{ }^\circ\text{C}$  the device shows dielectric constant ( $\epsilon'$ )  $\sim 330$  and achieved a maximum value of ( $\epsilon'$ )  $\sim 3445$  at  $100 \text{ }^\circ\text{C}$ , under the frequency condition of 100 Hz. It is evident from the figure that the  $\epsilon'$  value decreases with increasing frequency. The origin of high dielectric constant was due to the contribution

**Fig. 5** **A** Real part of dielectric constant ( $\epsilon'$ ) versus frequency curves, recorded under different temperature conditions, from 30 to 100 °C. **B** The variation of  $\tan(\delta)$  curves as a function of temperatures. **C** Arrhenius fitting of activation energy, extracted from the peak position of  $\tan(\delta)$  curves. **D** Linear variation of  $\epsilon''$  curves on log–log scale and **E** fitted slope ' $m$ ' value and the corresponding  $W_{\max}$  with respect to temperature



of space charge polarization and orientation polarization of dipoles within the measured frequency ranges. The organic–inorganic hybrid system was found to generate the structural defects or oxygen vacancies, leading to the creation of trap charges at the interface of the material [19, 43, 44]. For the current device, the trap charges are accumulated near the interface and produced space charge polarization towards low frequency region, resulted high value of dielectric constant (below 1 kHz). As the frequency increases, the space charges exhibit limited ability to align with the frequency direction, leading to a decrease in the polarization contribution and consequently resulting in a low value of the dielectric constant. Frequency above 1 kHz, the dielectric property is predominantly depending on orientation polarization of dipoles. Dipolar type of interaction in manganese stannate originated from the  $\text{SnO}_6$  and  $\text{MnO}_8$  units [45]. Each unit considered as a separate dipole consisting of Mn–O and Sn–O network, Fig. S1B (supporting information). These dipoles are aligned along the external field direction and contributed for the orientation polarization. A relaxation process occurs in these dipoles at a characteristic frequency ( $f_{\max}$ ), which is associated with a peak in the dielectric loss ( $\tan \delta$ ) curve, Fig. 5B. With rising temperature,  $\tan \delta$  peaks

are shifted towards higher frequency side (direction of arrow) and the behaviour was associated with a thermally activated process. The peak frequency ( $f_{\max}$ ) as function of temperature ( $1/T$ ) is plotted and fitted with the Arrhenius equation:  $f_{\max}^{Me} = f_0 \exp(-E_a/K_b T)$ , Fig. 5C. The activation energy value,  $E_a \sim 0.13$  eV, suggested the formation of polaronic charges either via long-range or short-range coulombic interaction between lattice ions. Similar behaviour has also been reported in other hybrid perovskite systems [46, 47]. The frequency dependent imaginary part of dielectric constant ( $\epsilon''$ ) under different temperature conditions are plotted in log–log scale, Fig. 5D. The linear behaviour of the curves indicates the polarization process was followed by hopping conduction mechanism [48]. The hopping contribution in the dielectric constant was estimated from the temperature dependent  $\epsilon''$  curves using Giuntini relaxation model [49],  $\epsilon'' = A\omega^m$ , ( $m < 0$ ), where  $m = -4K_B T/W_{\max}$ . The parameter  $A$  is a constant and temperature dependent factor. The exponential factor ' $m$ ' denotes the interaction between electrical dipoles, and  $W_{\max}$  is the maximum barrier height. Figure 5E displays the graphical representation of fitted  $\epsilon''$  curves (for all temperatures) with calculated slope ' $m$ ' and  $W_{\max}$ . The value of ' $m$ ' enhances with rising temperature

and maximum barrier height ( $W_{max}$ ), between the trap states, decreases with increasing temperature.

AC-conductivity ( $\sigma_{ac}$ ) of the MSO-based device was measured within the frequency range from 100 Hz to 1 MHz under different temperature conditions (30–100 °C), Fig. 6A, (semi-log scale). The conductivity curves display a change in slope at an intermediate frequency (above 10 kHz), marked by solid line, and separated into two regions, (I) and (II). Towards low frequency region (I), below 10 kHz, a weak plateau like feature followed by a weak frequency dependent behaviour was observed. In region (II), a considerable increase in the conductivity of the device was noticed and reached to a maximum value of  $\sigma_{ac} \sim 0.21$  S/m at 100 °C. The overall AC-conductivity behaviour is modelled according to the Jonscher’s power law,  $\sigma_{ac} = \sigma_0 + A(T)\omega^S$ , where  $\sigma_0$  is the frequency independent conductivity, A is the temperature dependent factor and the parameter ‘S’ determine the conduction

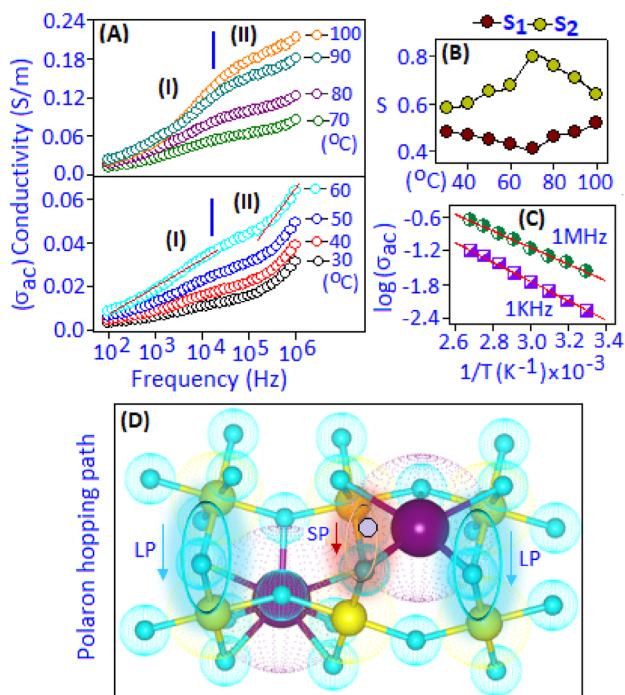


**Fig. 6** **A** AC-conductivity pattern of MSO-based device at different temperatures from 30 to 60 °C (bottom) and 70–100 °C (top). The curves are fitted according to the Jonscher’s power law (red line) for two different region I and II. **B** Variation of  $S_1$  and  $S_2$  parameters with temperature. **C** Activation energy ( $E_a$ ) plots at 1 kHz and 1 MHz, fitted (red line) according to the Arrhenius relation. **D** Hopping conduction path for large polaron (LP) and vacancy mediated small polaron (SP) inside the Sn–O lattice unit (Color figure online)

mechanism and the value varies in between  $0 < s < 1$ . The parameter  $S_1$  and  $S_2$  were extracted for regions (I) and (II), respectively, using the linear fitting of the Jonscher’s law and plotted the values as function of temperature in the Fig. 6B.

Different mechanisms have been proposed to explain the temperature and frequency dependent AC-conductivity of the charge carriers in the materials [50]. For the region (I), the  $S_1$  values were decreased with increasing temperature (between 30 and 70 °C) and then increased with increasing temperature (above 70 °C), such kind of behaviour is associated

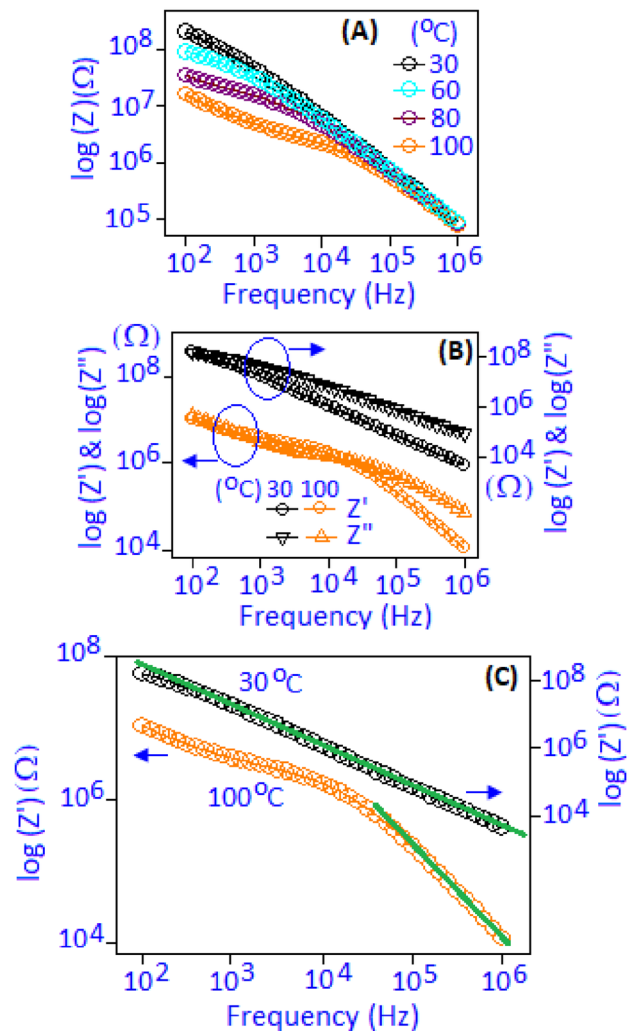


**Fig. 7** **A** Electrical impedance ( $Z$ ) versus frequency curve (log–log scale) at selected temperature (30, 60, 80 and 100 °C). **B** Variation of real ( $Z'$ ) and imaginary part ( $Z''$ ) of electrical impedance at selected temperature (30 and 100 °C) on a log–log scale. **C** Variation of real ( $Z'$ ) part of the electrical impedance of the device extracted at 30 °C and 100 °C. The solid line (green colour) shows the linearity of curves (Color figure online)

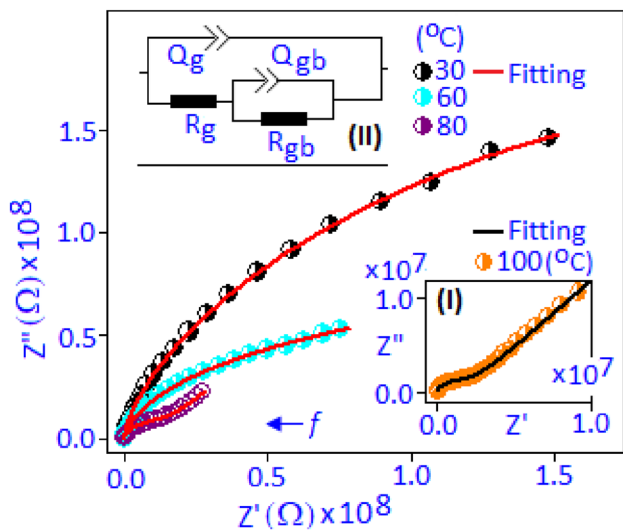


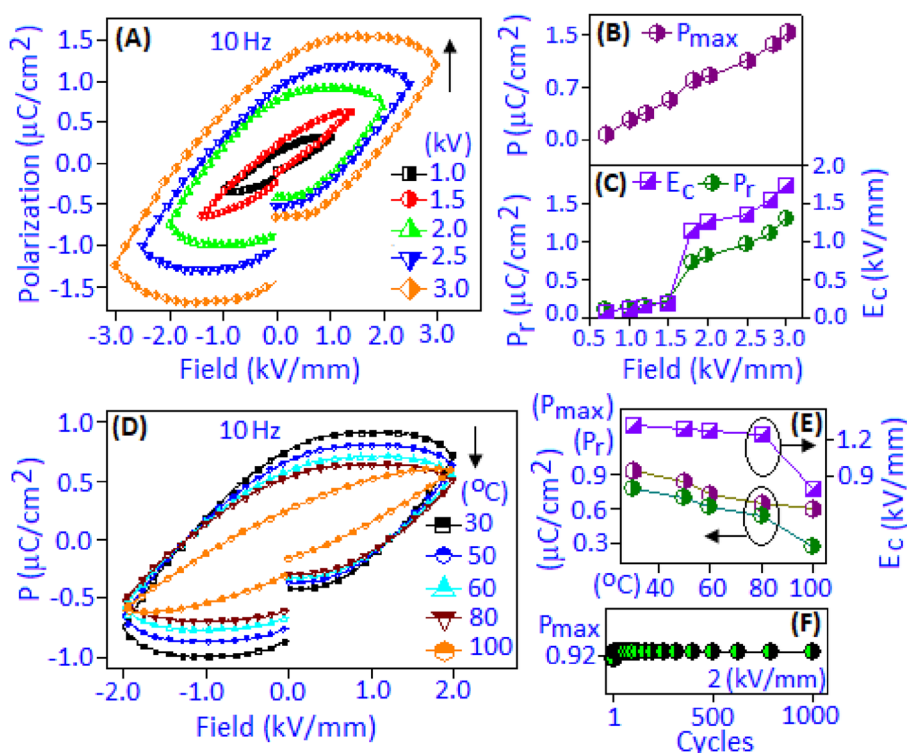
**Fig. 8** Main panel shows the Nyquist plots ( $Z'$  vs.  $Z''$ ) at selected temperature (30, 60, 80 °C) and inset (I) for 100 °C. The experimental curves are fitted according to the equivalent circuit model, inset (II)

with the overlapping large polaron tunnelling conduction process [44, 46, 51]. For the region (II), the  $S_2$  values were increased between 30 and 70 °C and then decreased with increasing temperature, above 70 °C, suggested the hopping contribution of small

polaron. The variation of AC conductivity ( $\sigma_{ac}$ ) as a function of temperature ( $1/T$ ) is represented by the Arrhenius relation;  $\sigma_{ac}(T) = \sigma_0 \exp(-E_a/K_B T)$ , where  $\sigma_0$  is a pre-exponential factor and  $E_a$  is the activation energy of the polaron for the regions (I) and (II). A linear fit of the above equation,  $\log \sigma_{ac}$  vs.  $1/T$ , delivers the value of  $E_a \sim 0.15$  eV and  $E_a \sim 0.12$  eV for two different regions (I) and (II) under the frequency condition of 1 kHz and 1 MHz, respectively, as illustrated in the Fig. 6C. Higher value of  $E_a$  for the region (I) is related to the formation of large polaron that migrate over long range distance. With increasing frequency, for region II, the motion is restricted within the localized state. The large polaron (LP) forms predominantly from the distorted  $\text{SnO}_6$  octahedra units and the oxygen vacancy-related formation of small polaron (SP) near the Sn–O bond, as illustrated in the Fig. 6D [46].

The electrical impedance ( $Z$ ) of the device under different temperature conditions (30, 60, 80 and 100 °C), are illustrated in the Fig. 7A (log–log scale). The  $Z$  value decreases with rising frequency and temperature. The real ( $Z'$ ) and imaginary ( $Z''$ ) part of the electrical impedance for selected temperatures (30 and 100 °C) are plotted in the Fig. 7B. At 30 °C, the linear variation of  $\log(Z')$  versus  $\log(f)$  with a slope value of  $\sim -0.81$ , over the entire frequency range, was

**Fig. 9** **A** Polarization–electric field (P–E) hysteresis pattern of MSO-based device, measured at 10 Hz. Arrow indicates the increment of P–E loop with applied electric field. Variation of **B**  $P_{max}$  and **C**  $P_r$  and  $E_c$  values with respect to the applied field. **D** Temperature dependent (30–100 °C) P–E loop and **E** the variation of  $P_{max}$ ,  $P_r$  and  $E_c$  values at 2 kV/mm applied field. **F** Room temperature polarization stability ( $P_{max}$ ) of the device under  $10^3$  switching cycles under applied field of 2 kV/mm





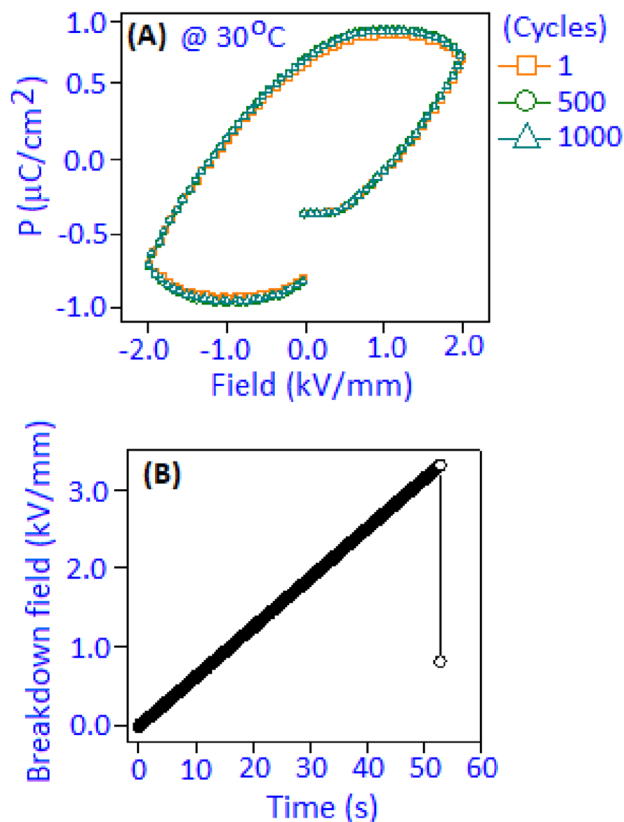


**Fig. 10** **A** P-E hysteresis loop performance of the device under repeated cycles (1, 500 and 1000) under  $\pm 2$  kV/mm field condition. **B** Electrical breakdown strength (kV/mm) of the device with respect to the time scale (s)

noticed, whereas a plateau like feature was more prominent towards low frequencies at 100 °C, Fig. 7C. Such behaviour in the  $Z'$  curve was originated from the contribution of space charges in the device.

Figure 8 exhibited the Nyquist plots (symbol), for selected temperatures (30, 60 80 and 100 °C), that extracted the individual contributions of nanoparticle (grain) and particle interfaces (grain boundary) for the electrical impedance. The device shows wide semi-circular arc at temperatures 30 °C and 60 °C, suggested an overlapping contribution of individual components. The Nyquist plot transformed into two semi-circular arc for the temperature 80 °C, Fig. 9 and for 100 °C, Fig. 9, inset (I). The smaller arc followed by larger arc were originated from nanoparticles and nanoparticles boundary effect, respectively. The experimental Nyquist plot were fitted (solid line) with an equivalent electrical circuit model, Fig. 9, inset (II). The circuit consists of two separate components,  $R_g Q_g$  and  $R_{gb} Q_{gb}$ , connected in parallel

combination. The first component  $R_g Q_g$  is related to the nanoparticle whereas, the second  $R_{gb} Q_{gb}$  component associated with particle boundary. The parameters R and Q correspond to resistive and capacitive components, respectively, of the MSO-based device. The component Q is considered as constant phase element (CPE) of the electrical circuit and related to the impedance ( $Z^*$ ) by the relation,  $Z_{CPE}^* = 1/(i\omega)^n Q$ , where,  $\omega$  is angular frequency and n is the exponential factor. For an ideal capacitor the value of  $n = 1$ , when  $n < 1$  that deviates to non-ideal capacitive element Q [52]. The extracted impedance parameters as listed in Table S2 (supporting information). At higher temperature, both capacitive components ( $Q_g, Q_{gb}$ ) values are increased and the resistive components ( $R_g$  and  $R_{gb}$ ) values are decreased. The localized conduction of polaronic charges, inside the particle, are more capacitive in nature, which significantly enhanced the  $Q_g$  values. The decrease of resistive values in the device with increasing temperature supported the thermally activated conduction process inside particles and the interfaces.

Polarization–electric field (PE) hysteresis loops of the device under various field conditions (1.0, 1.5, 2.0, 2.5 and 3.0 kV/mm) are illustrated in Fig. 9A, at 30 °C. The polarization of the device exhibited a direct relationship with the magnitude of the applied electric field. At the electric field of 3 kV/mm, the maximum polarization ( $P_{max}$ ) value  $\sim 1.5 \mu C/cm^2$  was achieved, Fig. 9B. The polarization hysteresis behaviour of the device was originated from the dipolar interaction of  $SnO_6$  and  $MnO_8$  polyhedra units. Each polyhedra consist of  $Mn^{\delta+}-O^{\delta-}$  and  $Sn^{\delta+}-O^{\delta-}$  dipoles, and the response of these dipoles along the field direction contribute to the hysteresis effect for the device. At initial field conditions ( $\leq 1.5$  kV/mm), the device exhibited unsaturated slim hysteresis loop due to inefficient applied field for dipole orientation. These dipoles retain their initial orientation and exert a restorative force opposing the external field, resulting in a narrow polarization hysteresis curve [53]. A step-like increment in the values of remanent polarization ( $P_r$ ) and coercive field ( $E_c$ ) were observed above an applied field of 1.5 kV/mm, Fig. 9C. Such kind of increment was originated due to the gradual increase of interaction of the non-aligned dipoles with strengthening of applied field. Figure 9D illustrates the temperature-dependent (30–100 °C) hysteresis pattern. The formation of oxygen vacancies and the defective dipoles were created in the device

**Table 1** The synthesis method, crystal structure and electrical properties of some reported stannate based materials

Material type	Synthesis condition	Crystal structure	Dielectric capacitance	Polarization performance	References
Polycrystalline Ti doped BaSnO <sub>3</sub> and PbSnO <sub>3</sub>	SSR(HT)	Cubic-BaSnO <sub>3</sub> tetragonal- PbSnO <sub>3</sub>	$\epsilon' \sim 40\text{--}83$	Spontaneous $P \sim 0.4 \mu\text{C}/\text{cm}^2$	[14]
Polycrystalline ZnSnO <sub>3</sub>	SSR (HT/HP)	Rhombohedral	–	Ferroelectric $P \sim 59 \mu\text{C}/\text{cm}^2$	[16]
Nano-composite ZnSnO <sub>3</sub> -polymer	Soft-chemical route	Rhombohedral	–	Dipolar polarization	[18]
Polycrystalline and thin film BaSnO <sub>3</sub>	SSR, MBE route	Cubic, Cubic	$\epsilon' \sim 90\text{--}120$ and $\epsilon' \sim 15\text{--}17$	–	[44, 54]
Polycrystalline Sb-doped BaSnO <sub>3</sub>	Thin film	Orthorhombic	–	Polarization $P \sim 40 \mu\text{C}/\text{cm}^2$ at 40 kV/mm	[55]
Polycrystalline Er doped SrSnO <sub>3</sub> (Sr <sub>1-x</sub> Er <sub>x</sub> SnO <sub>3-<math>\delta</math></sub> )	Sol-gel route	Orthorhombic	$\epsilon' \sim 10\text{--}50$ , phase transition	–	[56]
Hybrid Ag <sub>2</sub> SnO <sub>3</sub> , and Ag <sub>2</sub> SnO <sub>3</sub> -CN nanoparticles	Wet-chemical route	Orthorhombic	$\epsilon' \sim 445$ and $\epsilon' \sim 780$	$P \sim 0.05 \mu\text{C}/\text{cm}^2$ and $P \sim 0.31 \mu\text{C}/\text{cm}^2$	[19]
Polycrystalline MnSnO <sub>3</sub>	SSR (HP) and (HT)	Hexagonal, and rhombohedral	dielectric anomalies, $\epsilon' \sim 17$ (estimated)	Simulated $P \sim 55 \mu\text{C}/\text{cm}^2$	[21, 22, 24]
hybrid MnSnO <sub>3</sub> nanoparticles	WCR, ambient T/P	Orthorhombic	$\epsilon' \sim 330$ at 30 °C, $\epsilon' \sim 3445$ at 100 °C	$P \sim 1.5 \mu\text{C}/\text{cm}^2$ at 3 kV/mm	In this work

SSR solid state reaction, WCR wet-chemical route, MBE molecular beam epitaxy, HT high temperature, HP high pressure, T/P temperature/pressure

with rising temperature and that caused the reduction of  $P_{\text{max}}$ ,  $P_{\text{r}}$  and  $E_{\text{c}}$  values, Fig. 9E. The device maintained a stable  $P_{\text{max}}$  value of  $\sim 0.92 \mu\text{C}/\text{cm}^2$  over the repeated switching cycles under the applied field of 2 kV/mm, Fig. 9F. A fatigue free polarization was observed in the device at 30 °C for  $10^3$  cycles under the applied field of 2 kV/mm, Fig. 10A. However, the device showed electrical breakdown at  $\sim 3.3$  kV/mm and sustained the field for a period of 50 s, Fig. 10B. The presence of oxygen vacancies within the lattice potentially contributes to the formation of a conductive pathway, which offers a plausible explanation for the occurrence of electrical breakdown in the device. The synthesis method, crystal structure and electrical properties of some reported stannate based materials are presented in a tabular format (Table 1).

## 4 Conclusions

Orthorhombic crystal structure of manganese stannate nanoparticles with space group of  $Pnma$  has been synthesized by applying an organic-inorganic complexation mediated route. The structure included eightfold coordinated  $\text{Mn}^{2+}$  cation, surrounded by eight  $\text{O}^{2-}$  anions and formed  $\text{MnO}_8$  polyhedra unit. Each polyhedra unit interconnected through the corner-sharing  $\text{SnO}_6$  octahedra with the formation of a cage-like network. Microscopic analysis of manganese stannate particles displayed a cube-like morphology within the size range between 50 and 70 nm. Temperature and frequency dependent dielectric performances of manganese stannate based device exhibited maximum dielectric constant ( $\epsilon'$ ) value of  $\sim 3445$  at 100 °C and 100 Hz frequency condition. The high dielectric constant value was originated due to the contribution of space charge polarization and orientation polarization of dipoles within the measured frequency ranges. Temperature and frequency dependent AC-conduction mechanism of the manganese stannate-based device

involved both overlapping large polarons and non-overlapping small polarons. Electric field-dependent of polarization hysteresis loop of the device exhibited the maximum polarization value  $\sim 1.5 \mu\text{C}/\text{cm}^2$  under the electric field of 3 kV/mm. Under the applied field of 2 kV/mm, the device exhibited a fatigue-free polarization with a maximum value of  $\sim 0.92 \mu\text{C}/\text{cm}^2$ , sustained for  $10^3$  cycles under ambient temperature condition. The above results demonstrate that manganese stannate nanoparticle based device has the potential as a capacitor in microelectronic applications.

### Author contributions

SG investigated the material, writing the original draft and KM conceptualization, writing-review and editing.

### Funding

Open access funding provided by University of Johannesburg. This study was financially supported by the Faculty of Science, University Research Council, University of Johannesburg. Dr Harishchandra Singh (Nano and Molecular Systems Research Unit, University of Oulu, Finland) is also acknowledged for XPS analysis and helpful discussion.

### Data availability

Data will be made available on request.

### Declarations

**Conflict of interest** The authors declare no competing financial interest.

**Supplementary Information** The online version contains supplementary material available at <https://doi.org/10.1007/s10854-023-11156-5>.

**Open Access** This article is licensed under a Creative Commons Attribution 4.0 International License, which permits use, sharing, adaptation, distribution and reproduction in any medium or format, as long as you give appropriate credit to the original author(s)

and the source, provide a link to the Creative Commons licence, and indicate if changes were made. The images or other third party material in this article are included in the article's Creative Commons licence, unless indicated otherwise in a credit line to the material. If material is not included in the article's Creative Commons licence and your intended use is not permitted by statutory regulation or exceeds the permitted use, you will need to obtain permission directly from the copyright holder. To view a copy of this licence, visit <http://creativecommons.org/licenses/by/4.0/>.

### References

1. J.M. Wu, C. Xu, Y. Zhang, Y. Yang, Y.S. Zhou, Z.L. Wang, Flexible and transparent nanogenerators based on a composite of lead-free  $\text{ZnSnO}_3$  triangular-belts. *Adv. Mater.* **24**, 6094–6099 (2012)
2. G. Siddiqui, J. Ali, Y. Doh, K. Choi, Fabrication of zinc stannate based all-printed resistive switching device. *Mater. Lett.* **166**, 311–316 (2016)
3. V. Perla, S. Ghosh, K. Mallick, Role of carbon nitride on the resistive switching behavior of a silver stannate based device: An approach to design a logic gate using the CMOS–memristor hybrid system. *ACS Appl. Electron. Mater.* **5**, 1620–1627 (2023)
4. S. Heo, D. Yoon, S. Yu, J. Son, H. Jang, Non-volatile ferroelectric control of room temperature electrical transport in perovskite oxide semiconductor La:  $\text{BaSnO}_3$ . *J. Mater. Chem. C* **5**, 11763–11768 (2017)
5. A. Rovisco, A. Santos, T. Cramer, J. Martins, R. Branquinho, H. Águas, B. Fraboni, E. Fortunato, R. Martins, R. Igreja, P. Barquinha, Piezoelectricity enhancement of nanogenerators based on pdms and  $\text{ZnSnO}_3$  nanowires through microstructuration. *ACS Appl. Mater. Interfaces.* **12**, 18421–18430 (2020)
6. B. Padha, S. Verma, S. Arya, Fabric-based wearable self-powered asymmetric supercapacitor comprising lead-free perovskite piezoelectrodes. *Adv. Mater. Technol.* **7**, 2200079 (2022)
7. Y. Zulueta, R. Mut, S. Kaya, J. Dawson, M. Nguyen, Strontium stannate as an alternative anode material for Li-ion batteries. *J. Phys. Chem. C* **125**, 14947–14956 (2021)
8. M. Mohammad, W. Abdul Ghafor, Cadmium stannate thin film as a solar energy utilizing element. *Solid State Commun.* **88**, 227–230 (1993)
9. H. Mizoguchi, P. Woodward, C. Park, D. Keszler, Probing the electronic structures of ternary perovskite and

- pyrochlore oxides containing  $\text{Sn}^{4+}$  or  $\text{Sb}^{5+}$ . *J. Am. Chem. Soc.* **126**, 9796–9800 (2004)
10. W. Zhang, J. Tang, J. Ye, Photoluminescence and photocatalytic properties of  $\text{SrSnO}_3$  perovskite. *Chem. Phys. Lett.* **418**, 174–178 (2006)
  11. T. Truttman, F. Liu, J. Barriocanal, R. James, B. Jalan, Strain relaxation via phase transformation in high-mobility  $\text{SrSnO}_3$  films. *ACS Appl. Electron. Mater.* **3**, 1127–1132 (2021)
  12. H. Liu, J. Yang, H. Xiang, X. Gong, S. Wei, Origin of the superior conductivity of perovskite  $\text{Ba}(\text{Sr})\text{SnO}$ . *Appl. Phys. Lett.* **102**, 112109 (2013)
  13. W.W. Coffeen, Ceramic and dielectric properties of the stannates. *J. Am. Ceram. Soc.* **36**, 207–214 (1953)
  14. S. Nomura, Dielectric properties of titanates containing  $\text{Sn}^{4+}$  ions I. *J. Phys. Soc. Jpn.* **10**, 112–119 (1955)
  15. K. Ong, X. Fan, A. Subedi, M. Sullivan, D. Singh, Transparent conducting properties of  $\text{SrSnO}_3$  and  $\text{ZnSnO}_3$ . *APL Mater.* **3**, 062505 (2015)
  16. Y. Inaguma, M. Yoshida, T. Katsumata, A polar oxide  $\text{ZnSnO}_3$  with a  $\text{LiNbO}_3$ -type structure. *J. Am. Chem. Soc.* **130**, 6704–6705 (2008)
  17. H. Minato, K. Fujiwara, A. Tsukazaki, High-mobility field-effect transistor based on crystalline  $\text{ZnSnO}_3$  thin films. *AIP Adv.* **8**, 055327 (2018)
  18. K. Lee, D. Kim, J. Lee, T. Kim, M. Gupta, S. Kim, Unidirectional high-power generation via stress-induced dipole alignment from  $\text{ZnSnO}_3$  nanocubes/polymer hybrid piezoelectric nanogenerator. *Adv. Funct. Mater.* **24**, 37–43 (2014)
  19. S. Ghosh, V. Perla, K. Mallick, Improved capacitive performance and polarization sustainability of silver stannate nanoparticles: the role of carbon nitride incorporation. *ACS Appl. Electron. Mater.* **4**, 2032–2039 (2022)
  20. Z. Wang, Z. Wang, W. Liu, W. Xiao, X. Lou, Amorphous  $\text{CoSnO}_3@C$  nanoboxes with superior lithium storage capability. *Energy Environ. Sci.* **6**, 87–91 (2013)
  21. Y. Zhai, W. Wei, H. Hu, J. Jing, X. Lv, Y. Xu, J. Xie, Reduced graphene oxide decorated  $\text{CoSnO}_3@ZnSnO_3$  with multi-component double-layered hollow nanoboxes for high energy storage and capacity retention asymmetric supercapacitors. *J. Alloys Compd.* **857**, 157536 (2021)
  22. P. Saranya, S. Selladurai, Facile synthesis of  $\text{NiSnO}_3$ /graphene nanocomposite for high-performance electrode towards asymmetric supercapacitor device. *J. Mater. Sci.* **53**, 16022–16046 (2018)
  23. G. Gnanamoorthy, V. Yadav, V. Narayanan, Well organized assembly of (X)- $\text{CuSnO}_3$  nanoparticles enhanced photocatalytic and anti-bacterial properties. *J. Water Proc. Eng.* **36**, 101258 (2020)
  24. A. Aimi, T. Katsumata, D. Mori, D. Fu, M. Itoh, T. Kyomen, K. Hiraki, T. Takahashi, Y. Inaguma, High-pressure synthesis and correlation between structure, magnetic, and dielectric properties in  $\text{LiNbO}_3$ -type  $\text{MnMo}_3$  ( $M = \text{Ti}, \text{Sn}$ ). *Inorg. Chem.* **50**, 6392–6398 (2011)
  25. X. Hao, Y. Xu, C. Franchini, F. Gao, Covalent effects in magnetic ferroelectrics  $\text{MnMO}_3$  ( $M = \text{Ti}, \text{Sn}$ ). *Status Solidi B.* **252**, 626–634 (2015)
  26. S. Kang, First-principles analysis of ferroelectric transition in  $\text{MnSnO}_3$  and  $\text{MnTiO}_3$  perovskites. *J. Solid State Chem.* **262**, 251–255 (2018)
  27. P. Liu, Q. Hao, X. Xia, W. Lei, H. Xia, Z. Chen, X. Wang, Hollow amorphous  $\text{MnSnO}_3$  nanohybrid with nitrogen-doped graphene for high-performance lithium storage. *Electrochim. Acta.* **214**, 1–10 (2016)
  28. M. Wang, M. Lian, P. Zhu, H. Feng, High pressure synthesized ferroelectric  $\text{MnSnO}_3$  with high carrier mobility and the effects of ion implantation on structural and magnetic properties. *Phys. Lett. A.* **437**, 128089 (2022)
  29. A. Vegas, The  $\text{ASnO}_3$  ( $A = \text{Ca}, \text{Sr}$ ) perovskites. *Acta Cryst. B.* **42**, 167–172 (1986)
  30. E. Mountstevens, J. Attfield, S. Redfern, Cation-size control of structural phase transitions in tin perovskites. *J. Phys.: Condens. Matter.* **15**, 8315 (2003)
  31. E. Moreira, J. Henriques, D. Azevedo, E. Caetano, V. Freire, E. Albuquerque, Structural, optoelectronic, infrared and Raman spectra of orthorhombic  $\text{SrSnO}_3$  from DFT calculations. *J. Solid State Chem.* **184**, 921–928 (2011)
  32. N. Thomas, The compositional dependence of octahedral tilting in orthorhombic and tetragonal perovskites. *Acta Cryst. B.* **52**, 16–31 (1996)
  33. M. Johansson, P. Lemmens, Perovskites and thin films-crystallography and chemistry. *J. Phys. Condens. Matter.* **20**, 264001 (2008)
  34. J. Jaramillo, D. Tellez, J. Rojas, C. Vargas, E. Barrera, Synthesis of  $\text{LaYbO}_3$  perovskite through modified Pechini method: structural, electric and magnetic characterization. *Int. J. Mod. Phys. B.* **1**, 1550217 (2015)
  35. C. Lin, Y. Zhang, J. Liu, X. Li, Y. Li, L. Tang, L. Xiong, Pressure-induced structural change in orthorhombic perovskite  $\text{GdMnO}_3$ . *J. Phys.: Condens. Matter.* **24**, 115402 (2012)
  36. M. Tarrida, H. Larguem, M. Madon, Structural investigations of  $(\text{Ca}, \text{Sr})\text{ZrO}_3$  and  $\text{Ca}(\text{Sn}, \text{Zr})\text{O}_3$  perovskite compounds. *Phys. Chem. Minerals.* **36**, 403–413 (2009)
  37. X. Wu, S. Qin, L. Dubrovinsky, Investigation into high-pressure behavior of  $\text{MnTiO}_3$ : X-ray diffraction and Raman spectroscopy with diamond anvil cells. *Geosci. Front.* **2**, 107–114 (2011)

38. J. John, M. Dhananjaya, S. Suresh, S. Pillai, M. Sahoo, O. Hussain, R. Philip, V. Pillai, Effect of manganese doping on the structural, morphological, optical, electrical, and magnetic properties of BaSnO<sub>3</sub>. *J. Mater. Sci.: Mater Electron* **31**, 11159–11176 (2020)
39. H. Nesbitt, D. Banerjee, Interpretation of XPS Mn(2p) spectra of Mn oxyhydroxides and constraints on the mechanism of MnO<sub>2</sub> precipitation. *Am. Mineral* **83**, 305–315 (1998)
40. M. Oku, K. Hirokawa, S. Ikeda, X-ray photoelectron spectroscopy of manganese-oxygen systems. *J. Electron Spectros. Relat. Phenom.* **7**, 465–473 (1975)
41. M.C. Biesinger, B.P. Payne, A.P. Grosvenor, L.M. Lau, A.R. Gerson, R.C. Smart, Resolving surface chemical states in XPS analysis of first row transition metals, oxides and hydroxides: Cr, Mn, Fe, Co and Ni. *Appl. Surf. Sci.* **257**, 2727–2730 (2011)
42. H. Cho, T. Onozato, M. Wei, A. Sanchela, H. Ohta, Effects of vacuum annealing on the electron mobility of epitaxial La-doped BaSnO<sub>3</sub> films. *APL Mater.* **7**, 022507 (2019)
43. S. Ghosh, V. Perla, K. Mallick, Oxygen vacancy-controlled dielectric relaxation and field-driven polarization of bismuth-manganese bimetallic oxide nanoparticles: implications for capacitors. *ACS Appl. Nano Mater.* **7**, 7116–7124 (2021)
44. P. Singh, B. Brandenburg, C. Sebastian, P. Singh, S. Singh, D. Kumar, O. Parkash, Electronic structure, electrical and dielectric properties of BaSnO<sub>3</sub> below 300 K. *Jap. J Appl. Phys.* **47**, 3540–3545 (2008)
45. Y. Zhao, B. Yang, Q. Wu, Y. Zhou, F. Guo, S. Zhao, Oxygen polyhedral dipole-dipole interaction induced domain reconstruction and relaxor behaviors in layered perovskite films for dielectric energy storage. *Nanoscale* **13**, 16226–16233 (2021)
46. N. Tailor, N. Parikh, P. Yadav, S. Satapathi, Dielectric relaxation and polaron hopping in Cs<sub>2</sub>AgBiBr<sub>6</sub> halide double perovskites. *J. Phys. Chem. C.* **126**, 10199–10208 (2022)
47. D. Ghosh, E. Welch, A. Neukirch, A. Zakhidov, S. Tretyak, Polarons in halide perovskites: a perspective. *J. Phys. Chem. Lett.* **11**, 3271–3286 (2020)
48. S. Ouni, S. Nouri, H. Khemakhem, R. Hassen, Phase transitions, dielectric properties, and vibrational study of stannates perovskites Sr<sub>1-x</sub>Er<sub>x</sub>SnO<sub>3-δ</sub>. *Mater. Res. Bull.* **51**, 136–140 (2014)
49. J. Giuntini, J. Zanchetta, D. Jullien, R. Eholie, P. Houenou, Temperature dependence of dielectric losses in chalcogenide glasses. *J Non. Cryst. Solids.* **45**, 57–62 (1981)
50. S.R. Elliott, Ac conduction in amorphous chalcogenide and pnictide semiconductors. *Adv. Phys.* **36**, 135–217 (1987)
51. C. Franchini, M. Reticioli, M. Setvin, U. Diebold, Polarons in materials. *Nat. Rev. Mater.* **6**, 560–586 (2021)
52. S. Hajlaoui, I. Chaabane, K. Guidara, Conduction mechanism model, impedance spectroscopic investigation and modulus behavior of the organic-inorganic [(C<sub>3</sub>H<sub>7</sub>)<sub>4</sub>N][SnCl<sub>5</sub>(H<sub>2</sub>O)]•2H<sub>2</sub>O compound. *RSC Adv.* **6**, 91649–91657 (2016)
53. Z. Zhao, Y. Dai, F. Huang, The formation and effect of defect dipoles in lead-free piezoelectric ceramics: a review. *Sustain. Mater. Technol.* **20**, e00092 (2019)
54. W. Nunn, A. Prakash, A. Bhowmik, R. Haislmaier, J. Yue, J. Lastra, B. Jalan, Frequency- and temperature-dependent dielectric response in hybrid molecular beam epitaxy-grown BaSnO<sub>3</sub> films. *APL Mater.* **6**, 066107 (2018)
55. Q. Liu, J. Dai, Z. Liu, X. Zhang, G. Zhu, G. Ding, Electrical and optical properties of Sb-doped BaSnO<sub>3</sub> epitaxial films grown by pulsed laser deposition. *J. Phys. D: Appl. Phys.* **43**, 455401 (2010)
56. A. Kharrata, N. Moutiab, K. Khirounib, W. Boujelben, Investigation of electrical behavior and dielectric properties in polycrystalline Pr<sub>0.8</sub>Sr<sub>0.2</sub>MnO<sub>3</sub> manganite perovskite. *Mater. Res. Bull.* **105**, 75–83 (2018)

**Publisher's Note** Springer Nature remains neutral with regard to jurisdictional claims in published maps and institutional affiliations.